frontiers | Frontiers in Physics

TYPE Original Research
PUBLISHED 18 September 2024
DOI 10.3389/fphy.2024.1450631

OPEN ACCESS

EDITED BY
Nicolas Benech,
Universidad de la República, Uruguay

REVIEWED BY
Hui Chen,
Ningbo University, China
Howuk Kim,
Inha University, Republic of Korea

*CORRESPONDENCE
Sébastien Salles,
sebastien.salles@cnrs.fr

RECEIVED 17 June 2024
ACCEPTED 30 August 2024
PUBLISHED 18 September 2024

CITATION
Sauvage J, Moustefaoui S, Fiorentini S, Venet M, Fadnes S, Lovastakken L, Villemain O and Salles S (2024) Detection of natural pulse waves (PWs) in 3D using high frame rate imaging for anisotropy characterization.
Front. Phys. 12:1450631.
doi: 10.3389/fphy.2024.1450631

Detection of natural pulse waves (PWs) in 3D using high frame rate imaging for anisotropy characterization

Jack Sauvage[1], Safa Moustefaoui[1], Stefano Fiorentini[2], Maelys Venet[3,4], Solveig Fadnes[2,3], Lasse Lovastakken[2], Olivier Villemain[4,5] and Sébastien Salles[1,5,6]*

[1]Sorbonne Université, Centre National de Recherche Scientifique (CNRS), Institut National de la Santé Et de la Recherche Médicale (INSERM), Laboratoire d'Imagerie Biomédicale, Paris, France, [2]Department of Circulation and Medical Imaging (ISB), Norwegian University of Science and Technology (NTNU), Trondheim, Norway, [3]Department of Research and Innovation, Møre og Romsdal Hospital Trust, Ålesund, Norway, [4]Bordeaux University Hospital (CHU), Department of Pediatric and Adult Congenital Cardiology, Pessac, France, [5]Institut Hospital-Universitaire Liryc, Fondation Bordeaux Université, Centre National de Recherche Scientifique (CNRS), Institut National de la Santé Et de la Recherche Médicale (INSERM), Pessac, France, [6]University of Bordeaux, Centre National de Recherche Scientifique (CNRS), Centre de Resonance Magnetique, Centre de Résonance Magnétique des Systèmes Biologiques (CRMSB), Bordeaux, France

Introduction: Numerous studies have shown that natural mechanical waves have the potential to assess the elastic properties of the myocardium. When the Aortic and Mitral valves close, a shear wave is produced, which provides insights into tissue stiffness. In addition, the Atrial Kick (AK) generates a wave similar to Pulse Waves (PWs) in arteries, providing another way to assess tissue stiffness. However, tissue anisotropy can also impact PW propagation, which is currently underexplored. This study aims to address this gap by investigating the impact of anisotropy on PW propagation in a phantom.

Methods: Tube phantoms were created using Polyvinyl Alcohol (PVA). Anisotropy was induced between two sets of two freeze-thaw cycles by stretching and twisting the material. The study first tests and validates the procedure of making helical anisotropic vessel phantoms using the shear wave imaging technique (by estimating the shear wave speed at different probe angles). Using plane wave ultrasound tomography synchronized with a peristaltic pump, 3D high frame rate imaging is performed and used to detect the 3D propagation pattern of PW for each manufactured vessel phantom. Finally, the study attempts to extract the anisotropic coefficient of the vessel using pulse wave propagation angle.

Results: The Shear wave imaging results obtained for the isotropic vessel show very similar values for each probe angle. On the contrary, the results obtained for the axial anisotropy vessel show a region with a higher shear wave speed at about 0°, corresponding to the long axis of the vessel. Finally, the results obtained for the helical anisotropy depicted increasing shear wave velocity value from −20° to 20°. For the axial phantom, the wavefront of the pulse wave is perpendicular to the long axis of the vessel, while oriented for the helical anisotropic vessels phantom. The pulse wave propagation angle increased with the number of twists made during the vessel manufacturing.

Discussion: The results show that anisotropy can be induced in PVA vessel phantoms by stretching and twisting the material in freeze-thaw cycles. The

findings also suggest that vessel anisotropy affects pulse wave propagation angles. Estimating the pulse wave propagation angle may be interesting in characterizing tissue anisotropy in organs where such waves are naturally present.

KEYWORDS

cardio-vascular, ultrafast ultrasound imaging, pulse wave, anisotropy, vessel phantom

1 Introduction

Cardiovascular diseases (CVDs) are a major cause of mortality around the world and pose significant challenges to global healthcare systems. Early-stage diagnosis is crucial for patients suffering from CVDs [1]. The mechanical properties of the myocardium, play a key role in the overall cardiac performance [2]. Alterations in myocardial elasticity can indicate pathological conditions, such as myocardial infarction, fibrosis, hypertrophy, or myocardial ischemia [2]. Additionally, tissue remodeling can affect the cardiac fiber orientation, which could serve as a pathological marker [3]. In recent years, ultrasound imaging has emerged as a powerful non-invasive modality for evaluating cardiovascular stiffness. Shear Wave Elastography (SWE), which relies on the propagation of shear waves generated by radiation forces from an acoustic push, has been used to retrieve tissue elasticity in several cardiac applications in humans. For instance, SWE was used to quantify stiffness in hypertrophic cardiomyopathy adults [4], healthy children [5], and patients with conduction delays [6]. SWE was also used to evaluate stiffness in various vascular applications. It has been used to evaluate the stiffness of the carotid artery [7] and on patients with spontaneous coronary artery dissection [8] or to evaluate atheroma plaque [8].

The elastic properties of the cardiovascular tissue can also be characterized by natural mechanical waves [6–8] The closure of aortic and mitral valves generates a shear wave that can be used to estimate tissue stiffness [9, 10] and anisotropy [11], i.e., cardiac fiber orientation. Similarly, the Atrial Kick (AK) generates a wave comparable to Pulse Waves (PWs) in the arteries, which can also be used to characterize tissue stiffness [12, 13]. In [14], we show the possibility of estimating and reconstructing the trajectory of such waves in the left ventricle in 3D.

To the best of our knowledge, PW has only been used to determine vessel stiffness. High-frame rate ultrasound imaging has been used to quantify vessel stiffness *in vitro* and retrieve the incremental Young modulus via the Moense-Korteweg equation [15–17]. PWI (pulse wave imaging) has been used to measure carotid artery stiffness *in vivo* in healthy subjects [18, 19] and stenosis patients [20]. PW velocity has also been estimated using a 2D matrix array on a healthy carotid artery *in vivo* [21]. In previous work, we demonstrated on a single phantom with 2D high frame rate imaging that anisotropy may affect the pulse wave propagation [22].

There is limited knowledge available on the use of PW imaging for estimating tissue anisotropy. The main aim of this study is to investigate the impact of anisotropy on PW propagation in vessel phantoms. The process of creating an anisotropic vessel phantom is explained and tested with the SWE technique. Using plane wave ultrasound tomography, synchronized with a peristaltic pump, the 3D propagation pattern of PW is reconstructed and compared between vessels phantom with different induced anisotropy. Finally, a preliminary attempt is made to determine an anisotropy coefficient from the pulse wave propagation.

2 Materials and methods

2.1 Phantom manufacturing

The study was conducted using cylindric phantoms composed of polyvinyl alcohol (PVA). PVA has been chosen for his ability to change his mechanic properties with freeze-thaw cycles. The stiffness of a PVA phantom can be changed according to the number of freeze-thaw cycles [23], and fibers can be introduced by applying strain during the freeze-thaw cycle [24]. The different phantom models were created through the following process: A blend consisting of 10% w/v polyvinyl alcohol powder (MW 85 k–124 k, Sigma Aldrich, United States), 89% w/v water, and 1% w/v silica gel (mesh size 230–400, 40–63 µm, Supelco, Sigma Aldrich, Bosnia-Herzegovina) was heated to 90°C and stirred until the PVA powder completely dissolved [25]. After degassing, the solution was allowed to cool to 25°C. Subsequently, any remaining air bubbles were removed from the surface, and the solution was poured into the mold.

The mold is a 300 mm-long cylinder with an internal diameter of 13 mm. An 8 mm-diameter filled cylinder was used to create the lumen (Figure 1). The phantoms first underwent two freeze-thaw cycles. Each cycle consisted of a 24-h freeze period at −20°C ± 0.5°C and a 3-h thaw period at 16°C ± 0.5°C. Following the methodology described in [26], axial and shear strains were induced in the phantoms to achieve anisotropy by creating fiber in the desired direction.

A first batch was used for anisotropy validation using SWE. Axial anisotropy was induced in the first phantom by stretching it a factor of 1.6 of its initial length with a final length of 21 cm. The second phantom was induced with helical anisotropy by first stretching it by a factor of 1.6 of its initial length and then twisting it by two complete turns, with a final length of 18.5 cm. To make anisotropy permanent, both phantoms underwent two additional freeze-thaw cycles while being kept in their deformed state. An isotropic vessel phantom has been made with the same procedure but without any stretching or twisting.

A second batch was used for the PW imaging investigation. It consists of one isotropic and three helical anisotropy phantoms. The three helical anisotropy phantom was made by stretching it by a factor of 1.6 of its initial length and then twisting it by one, two, and three complete turns, respectively. Finally, the phantoms were placed in a water tank.

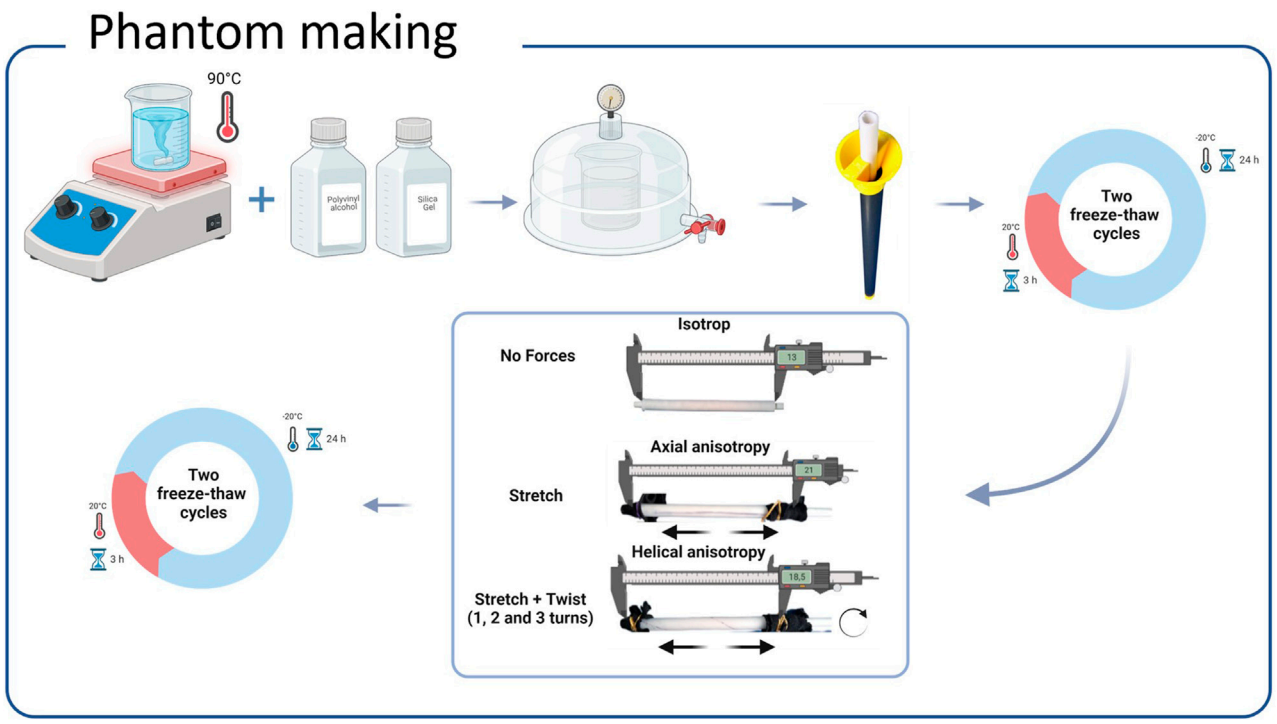

FIGURE 1
PVA phantom-making procedure. A blend consisting of 10% w/v polyvinyl alcohol powder 89% w/v water, and 1% w/v silica gel was heated to 90°C. After degassing, the solution was allowed to cool to 25°C. Subsequently, any remaining air bubbles were removed from the surface, and the solution was poured into a mold. The phantoms underwent two freeze-thaw cycles. Then axial and shear strains were induced in the phantoms to achieve anisotropy by creating fiber in the wanted direction. Finally, the phantoms underwent two additional freeze-thaw cycles while being kept in their deformed state.

2.2 Anisotropy validation using shear wave elastography

We validated the procedure of making the anisotropy with SWE. The same methodology described in [26] has been used to retrieve the fiber direction. The radiation force of a focused ultrasound beam has been used to induce shear waves in the vessel phantom with the L7-4 probe connected to the Vantage 256 (Verasonics Inc., Kirkland, Washington, United States).

Each pushing beam with a duration of 120 ms was followed with high frame rate imaging made single plan wave at 0°, reaching 10,000 fps. The ultrasound probe attached to a rotation device was rotated from −20° to 20° at 5° increments. Ten shear wave events have been produced and processed for each increment.

The motion induced by the shear wave was estimated using conventional Tissue Doppler imaging (TDI). TDI was implemented by taking the phase of lag-one autocorrelation $\widehat{\Re}_x$ of the IQ signal, to assess the axial velocity V given by Equations 1, 2:

$$\hat{V} = \frac{\angle \widehat{\Re}_x(1) \times vNyq}{\pi} \tag{1}$$

where the Nyquist velocity $vNyq$ follows the expression:

$$vNyq = \frac{C_0 \times PRF}{4 f_0} \tag{2}$$

where C_0 is the sound speed (1540 m/s), and f_0 is the transducer center frequency (5.2 Mhz).

After taking an anatomical M-mode along the vessel wall, 2D spatial-temporal maps was extracted and used to estimate the shear wave speed (Figure 2) For each shear wave event, the 1D (along the M-mode line) time of flight of the shear wave was estimated automatically by detecting the maxima of the tissue velocity in the space-time dimensions. The shear wave speed has been extracted from the linear regression of the detected maxima.

2.3 Pulse wave tomography imaging

2.3.1 High frame rate imaging

Radio Frequency (RF) channel data were acquired using a Vantage 256 scanner system (Verasonics) equipped with an L7-4 probe. The ultrasound probe was positioned perpendicular to the vessel's long axis. The acquisition sequence consisted of non-compounded plane waves fired at 2.5 kHz Pulse Repetition Frequency (PRF). The total acquisition time for each cross-section was 2s or 10,000 frames. RF channel data were demodulated and beamformed using a conventional delay and sum technique available in the USTB [26].

2.3.2 Pulse wave tomography

The pulse wave was induced by connecting the vessel's phantom, placed in a water tank, to a peristaltic pump (Masterflex, Avantor). The L7-4 probe was attached to a translational device controlled by the Vantage computer and synchronized to the ultrasound acquisition. After each acquisition of 2s the data were saved together with the

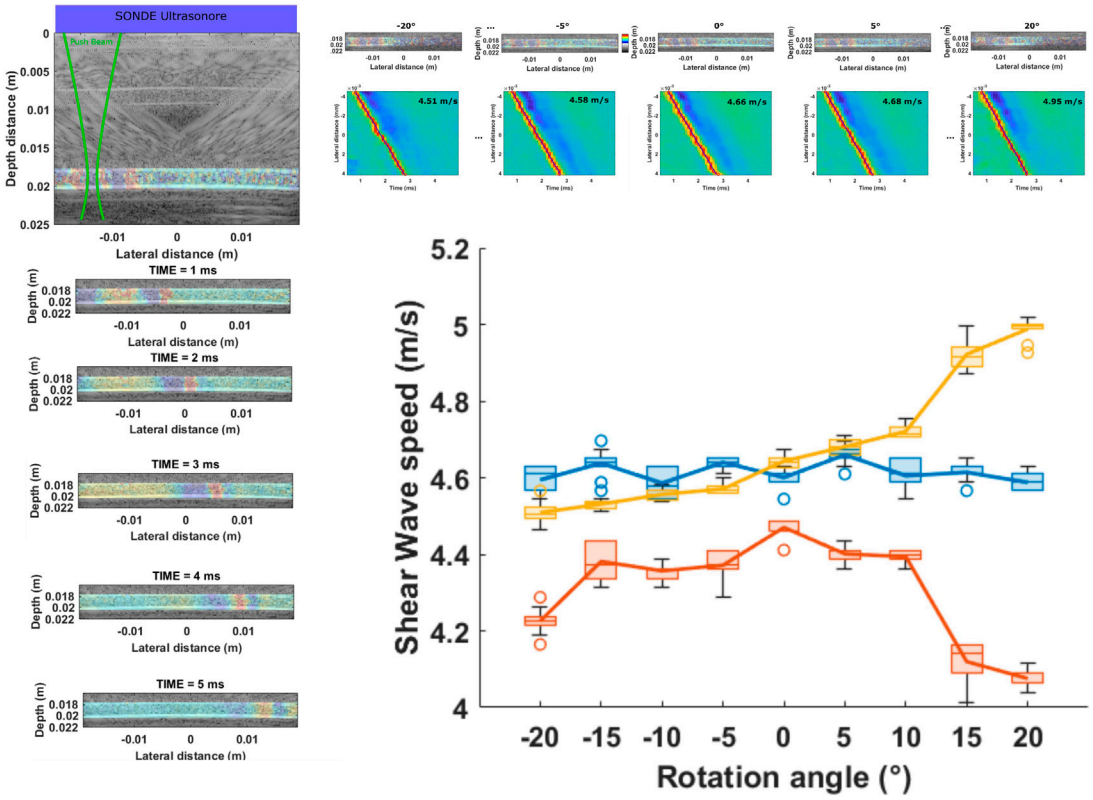

FIGURE 2
Shear wave experiment. The radiation force of a focused ultrasound beam has been used to induce shear waves in the vessel phantom. The ultrasound probe was rotated from −20° to 20° at 5° increments. The estimated tissue motion is displayed on the left of the figure from 1 ms to 5 ms. A 2D spatial-temporal map extracted at the lower vessel wall is shown at the top of the figure for five rotational angles. The shear wave speed estimated for the Axial (in red), helical (in yellow), and isotropic (in blue) phantom is displayed for the eight investigated angles. The results obtained for each 10-shear wave event are represented as a box plot for each rotational angle. The results obtained for the isotropic vessel show very similar values for each angle. On the contrary, the results obtained for the axial anisotropy vessel show a region with a higher shear wave speed of about 0°, corresponding to the long axis of the vessel. Finally, the results obtained for the helical anisotropy depicted increasing shear wave velocity value from −20° to 20°.

acquisition timing, then followed by a probe translation of 0.58 mm. The process was repeated 45 times while the peristaltic pump ran continuously. The 45 cross-sectional acquisitions were synchronized offline with a Pump signal (Figure 3).

2.3.3 Pulse wave tracking

Tissue motion induced by PW propagation was detected using TDI. Tissue acceleration curves were estimated as the time derivative of TDI, smoothed using a 5 × 5 samples spatial moving average filter (0.74 mm × 0.74 mm) and a 20 samples temporal moving average filter (4 ms). The foot of the PWs was defined as the inflection point, where the temporal derivative of the velocity (i.e., wall acceleration) attains its maximum before the peak velocity. Therefore, the PW time of arrival for each spatial point on the cross-section was found by detecting the maximum of the tissue acceleration curves. The search was limited to a 12 ms temporal window or 60-time samples. Because the upper and lower walls have a velocity in the opposite directions, the results were produced separately for the positive and negative velocity components (Figure 3). The spatial-temporal maps have been extracted by detecting the maxima of the tissue acceleration at all points within the vessel phantoms in 3D. To simplify the visualization of the wave propagation timing, a 2D spatial-temporal map was extracted from the 3D volumes by taking a cylinder in the middle of the vessel wall (Figure 3).

2.3.4 Wave propagation assessment

The 2D spatial propagation time difference has been estimated with the 2D spatial gradient method. The results are then depicted as arrows showing the local wave propagation direction. Note that the vectors do not represent velocity but time over space and its amplitude is expressed in s/m, which we conveniently called the inverse speed. In this study, we proposed to use this inverse speed vector to describe the pulse wave propagation. For instance, a plane wave propagating in a homogenous medium will have an inverse speed of zero perpendicular to its propagation and an inverse speed different from zero in the direction of the propagation. Hence, the inverse speed vector will point out the main axis of the wave propagation. Here, we propose to extract the local angle of the inverse speed to characterize the wave propagation direction.

3 Results

3.1 Shear wave results

The shear wave results can be found in Figure 2. The results obtained for each 10-shear wave event are represented as a box plot for each rotational angle. The results obtained for the isotropic vessel

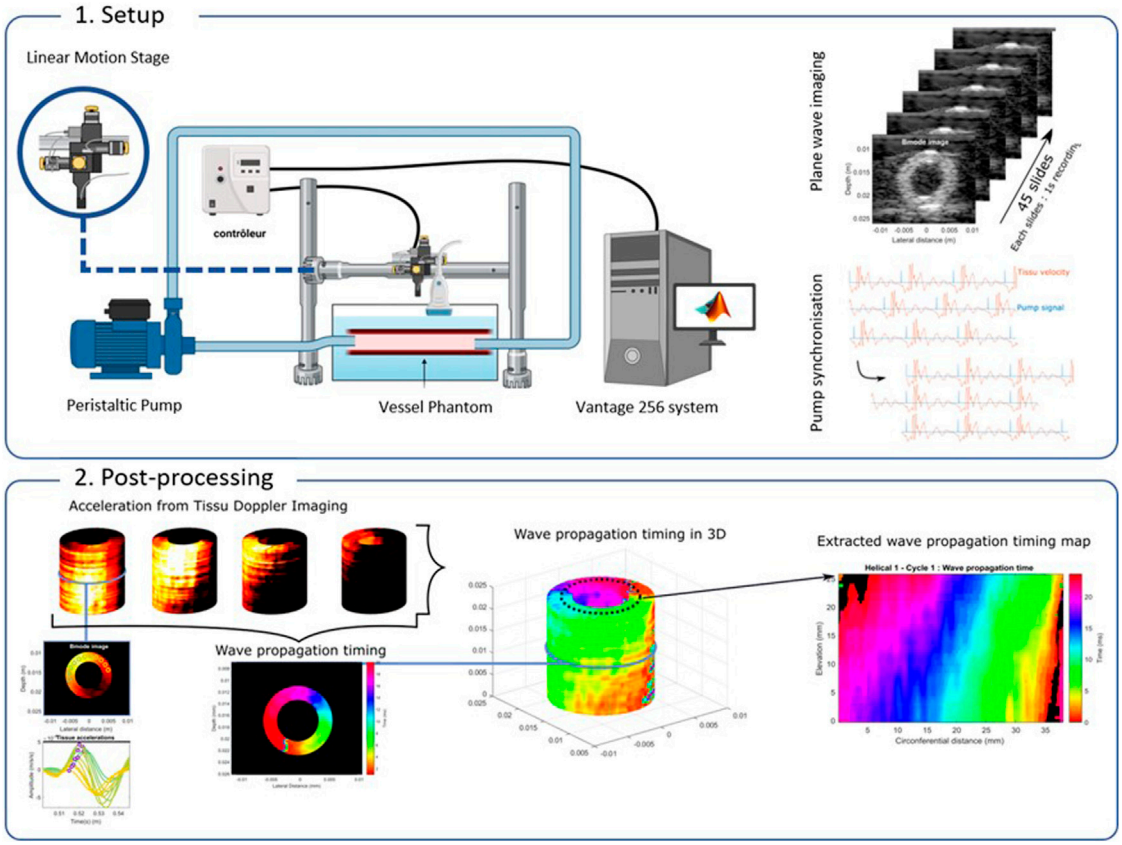

FIGURE 3
Pulse wave tomography. 1. The pulse wave was induced by connecting the vessel's phantom, placed in a water tank, to a peristaltic pump. The L7-4 probe was attached to a translational device controlled by the computer. 45 cross-sectional acquisitions were saved and synchronized offline with a Pump signal. 2. Tissue motion induced by PWs propagation was detected TDI. The wave propagation timing was estimated by detecting the maximum of the tissue acceleration from TDI. Tissue acceleration curves were estimated as the time derivative of TDI. Then, to simplify the visualization and processing of the wave propagation timing, a 2D spatial-temporal map has been extracted from the 3D volumes by taking a cylinder in the middle of the vessel wall.

(in blue) show very similar values for each probe angle, with a standard deviation of ±0.04 m/s, indicating a homogeneous shear wave propagation speed. On the contrary, the results obtained for the axial anisotropy vessel (in red) show a region with a higher shear wave speed at about 0°, corresponding to the long axis of the vessel. Finally, the results obtained for the helical anisotropy depicted increasing shear wave velocity value from −20° to 20°. Knowing that the wave speed of the wave is supposed to be higher in the fiber direction [24]. The results suggest that anisotropic structure have been introduced along the long axis of the vessel and with a certain angle for the axial and helical anisotropy phantom, respectively.

3.2 Pulse wave imaging results

Examples of the estimated tissue acceleration in 2D for one cross-section and for each type of phantom are shown in Figure 4. Differences can be found between the two types of phantoms. While no delay can be found between each tissue acceleration for the axial anisotropy phantom, the helical anisotropic phantoms exhibited a delay between each tissue acceleration. By extracting the timing of the maximum acceleration, the time of flight map was produced. For the axial anisotropic phantom, the results indicated that the pulse wave arrives at the cross-section almost at the same time with no delay between the positive and negative components of the motion induced but the pulse wave. On the other hand, temporal gradient can be found spatially all around helical vessel phantoms. This indicates that the pulse wave arrived with a delay at the cross section in a helical fashion. These results also show that the positive and negative components of the motion induced by the wave are following each other, turning all around the phantom.

3D volume rendering was produced after the synchronization of each cross-section with the Pump signal, as shown in Figure 3. To better appreciate and compare the wave propagation pattern, the timing of the maximum acceleration found in a cylinder located in the middle of the wall vessel has been extracted and shown in 2D space. Resulting in a 2D spatiotemporal map representing the TOF of the PW over elevation and circumferential distances. The extracted TOF maps for the four different phantoms are depicted in Figure 5 separately for the negative and positive components. To better see the differences the same dynamic range has been used for each case. For the axial phantom, the wavefront of the pulse wave is perpendicular to the long axis of the vessel, indicating that the pulse wave direction follows the long axis of the vessel, for both positive

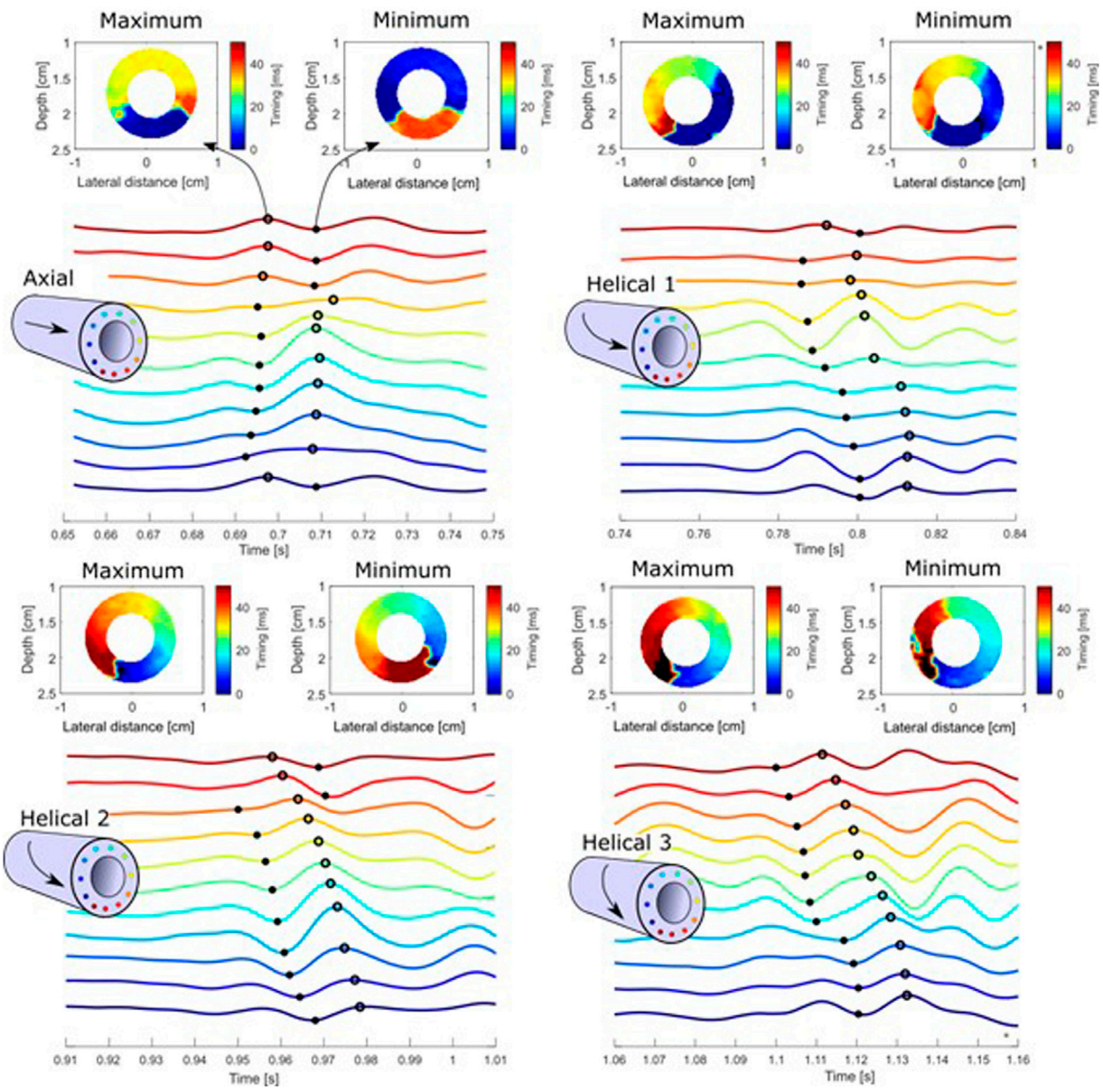

FIGURE 4
Pulse wave propagation in 2D cross-sectional slices. The pulse wave arrival time at a section is shown for the Axial and Helical 1, 2, and 3 phantoms. Examples of tissue acceleration taken at equidistance all around the vessel wall (indicated by different colors) are depicted at the bottom of each case. The detection of the maxima and minima of the acceleration is depicted with a dot and a circle, respectively. The colors depicted in the cross-section represent the timing of the maxima or minima taken at each position in the vessel walls.

and negative components. As expected, the positive component of the motion induced by the wave was detected on top of the phantom, whereas the negative component was detected at the bottom. The propagation pattern exhibited by the three helical cases is markedly distinct. The wavefront is not perpendicular to the long axis of the wall but oriented. Given that the mechanical wave propagates in a perpendicular direction relative to the wavefront, this result corroborates the hypothesis that the pulse wave direction is locally oriented. Moreover, while the time difference does not appear to vary significantly between the cases in the elevation direction, it does increase significantly in the circumferential direction. The results indicate that the pulse wave direction is influenced by the tissue anisotropy.

The average values of the propagation time amplitude and angle are presented in Figure 6. While the propagation time amplitude in the elevation direction (along the long axis of the vessel) appears to be relatively consistent across different vessel phantoms, the propagation time amplitude in the circumferential direction increases with the number of circumferential turns made during vessel manufacturing. As expected from the observation made in

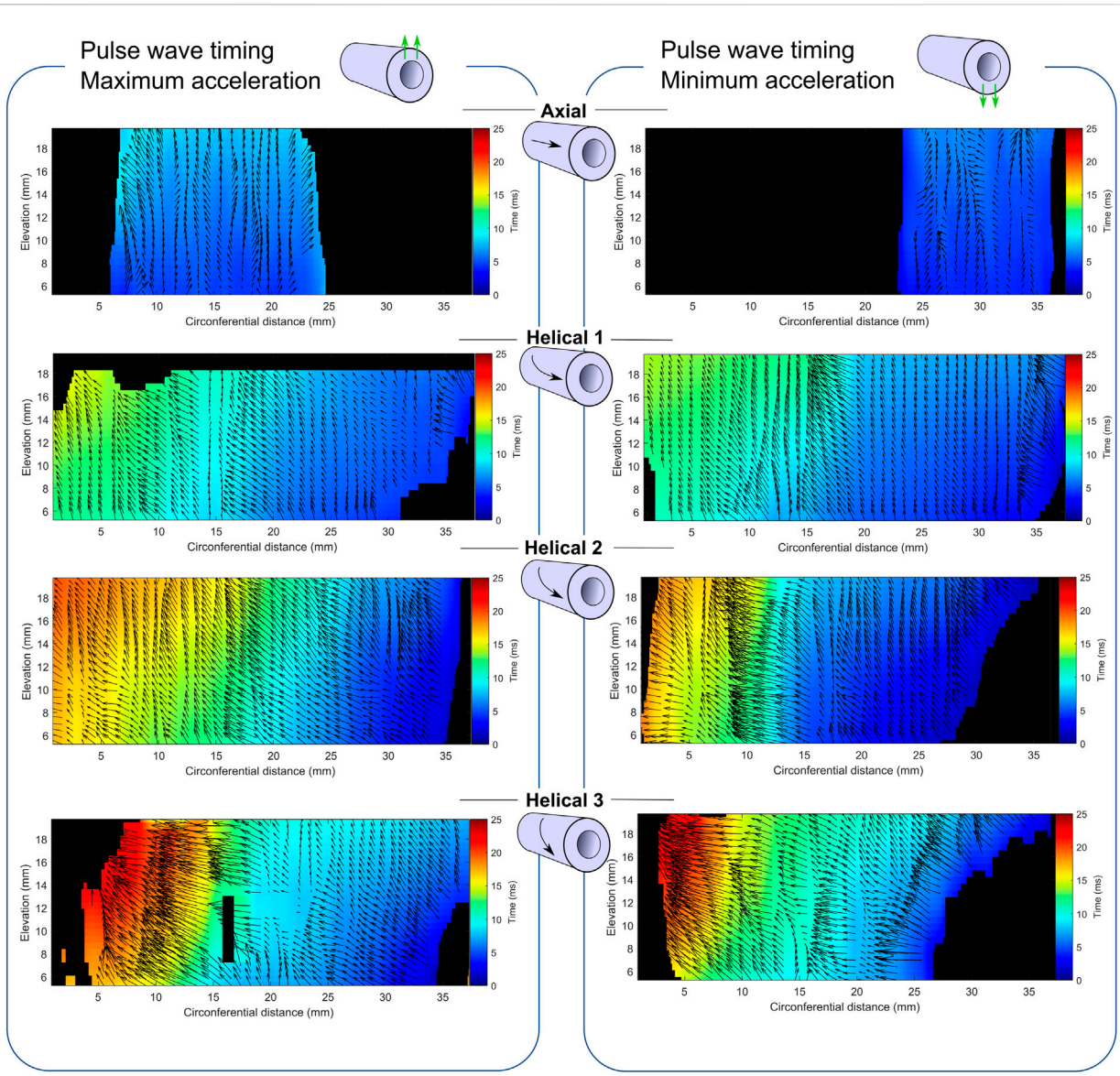

FIGURE 5
Pulse wave propagation in 3D. Relative time-of-arrival of the PW for the axial and helical anisotropic phantoms depicted from the detection of the maxima the minima of the tissue acceleration. The maps extracted from a cylinder located in the middle of the wall vessel show the PW propagation in a 2D space (elevation vs. circumferential direction). Black arrows have been added to the top of the maps describing the 2D spatial gradient. The black regions correspond to either too low acceleration amplitude, or out of range timing.

Figure 5 the propagation time angle increases with the number of circumferential turns.

4 Discussion

In this work, we evaluated the influence of tissue anisotropy on the pulse wave propagation in vessel phantom. The main conclusions of this study are: i) anisotropy can be induced in PVA vessel phantoms, ii) The pulse wave propagation is affected by vessel anisotropy, and iii) The angle of the wave propagation main axis increases with the number of circumferential turned made during vessel manufacturing and suggest that pulse wave propagation could be used evaluated tissue anisotropy.

Anisotropy has been introduced by creating fibers in different directions. The fibers were introduced by applying forces during the freezing cycles of PVA phantom-making. Axial anisotropy has been introduced by stretching, whereas helical anisotropy has been introduced by stretching and twisting the vessel phantom. Introducing a certain anisotropy with this procedure was a simple task due to the small vessel thickness and the small amount of force needed to stretch and twist the phantom properly. However, we did not have enough control over the spatial consistency of the introduced anisotropy, which can be seen as a major limitation of the presented procedure. Hence, the inconsistency of the introduced anisotropy could explain the propagation time angle variation depicted in Figures 5, 6.

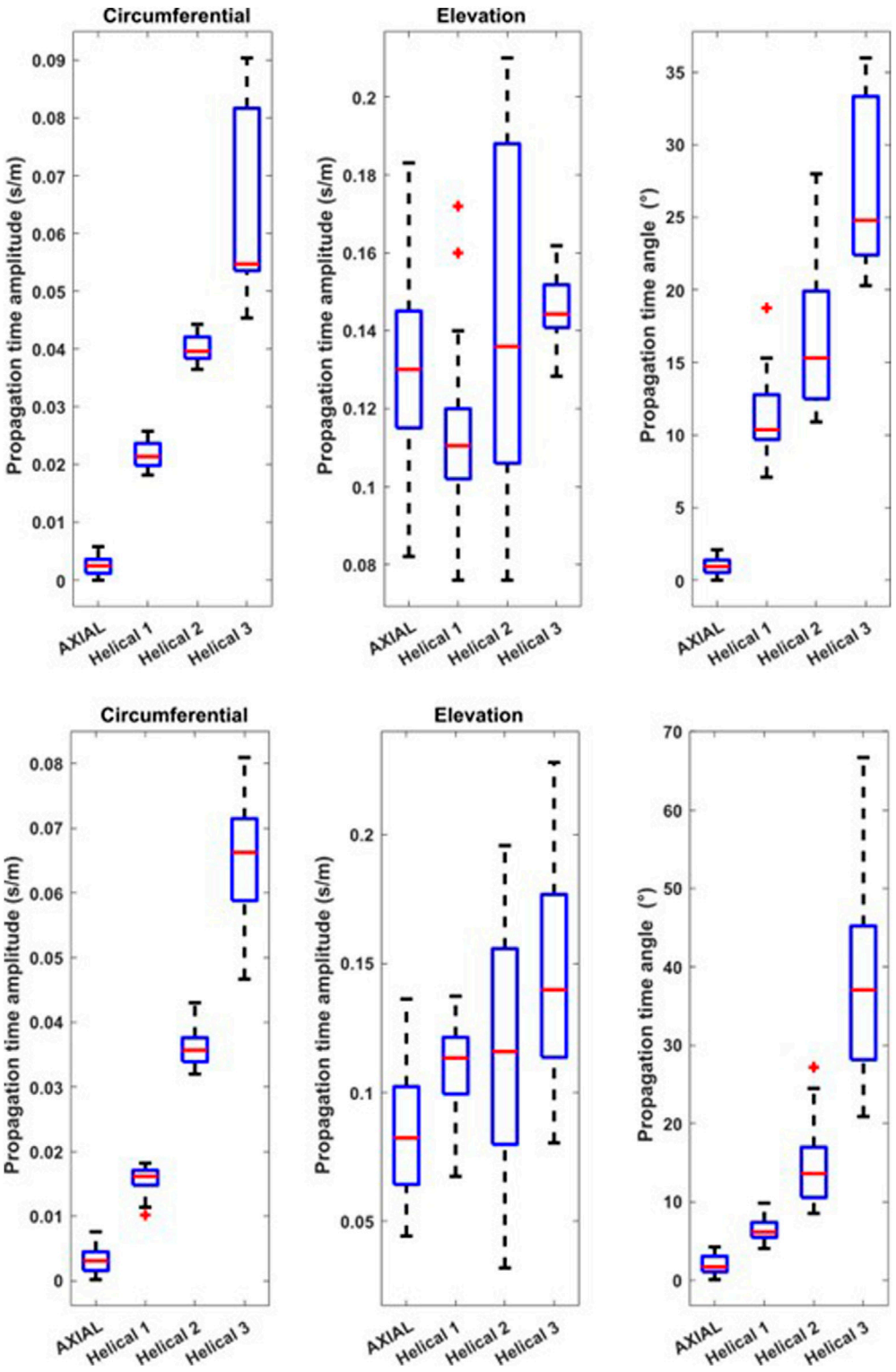

FIGURE 6
Propagation Time Amplitude and angle. The propagation time amplitude in the circumferential and elevation direction are depicted together with the angle from the detection of the maxima (on top) and the minima (at the bottom) of the tissue acceleration.

The tissue anisotropy was evaluated using shear wave imaging. Following the procedure described in [26], we estimated the shear wave speed at different probe orientation angles. The wavelength of the induced shear wave is larger than the wall thickness of the vessel, making the shear wave strongly dispersive and guided within the vessel wall. Hence, depending on the angle of the probe, the so-called guided circumferential wave or guided longitudinal wave could be detected [27], contradicting the results. We limited the orientation

angle at −20° to 20 to focus only on the guided longitudinal wave. This limitation does not allow us to correctly find the fiber angle for the helical phantom. However, clear differences between the isotropic, axial, and helical phantom have been observed which confirms that that we manage to induce fiber in the wanted direction.

The pulse wave produced a motion perpendicular to the tangent to the vessel. In this study, the motion induced by the pulse wave has been estimated along the ultrasound field direction only; hence, the amplitude of the estimated motion will depend on the position around the vessel, deteriorating the wave detection on the right and left sides of the vessel. 2D motion estimation, such as vector Doppler [27] or TO method [28], could help to better detect the motion induced by the wave in 2D.

First, the PW propagations were observed with the relative time of arrival over a cross-section (Figure 4). For the axial case, the pulse wave arrived at the same time at the section with positive and negative acceleration, i.e., maximum and minimum acceleration, respectively, on top and at the bottom of the vessel. For this phantom, the results did not show a perfect separation between the positive and negative acceleration at an equal distance from the middle. This can be attributed to the fact that the estimated tissue acceleration is relatively low on the sides of the phantoms, which can make it challenging to distinguish between positive and negative components. For the helical cases, Helical 2 and 3 exhibit clear temporal gradients throughout the cross-section, whereas Helical 1 exhibits temporal gradients only in the left area. This could be due to either a misdetection detection of mechanical waves or manufacturing inaccuracies.

After the synchronization of the 45 cross-section acquisitions, the 3D PW propagation was analyzed by extracting a 3D TOF map from the 3D volumes and computing the spatiotemporal gradient map (Figure 5). The amplitude of the gradient expressed in s/m gives information regarding the time that takes the PW to travel a unit distance. This time propagation has been depicted in both circumferential and elevation directions. For instance, for the axial vessel phantom, the propagation time amplitude in the circumferential direction is very close to zeros, indicating no propagation in this direction. On the other hand, in the elevation direction, the propagation time amplitude is around 0.12 s/m, indicating wave propagation in this direction. As expected, the propagation time in the circumferential direction increased with the number of circumferential turns during vessel manufacturing. In the elevation direction, the propagation time amplitude remained fairly constant across the vessel's phantom, indicating a constant stiffness in this direction expected from the same number of freeze-thaw cycles used for each phantom. We proposed to use the angle of the propagation time vectors as an anisotropy coefficient. As expected, the propagation time angle increases with the number of circumferential turns during vessel manufacturing.

Because the pulse wave propagation time vector angle changed with the number of circumferential turns made during vessel manufacturing and that the number of circumferential turns should be linked to the degree of anisotropy, i.e., fiber angle, we suggest that the pulse wave propagation time vector could be used to quantify the anisotropy of the vessel wall.

It is interesting to note that the pulse wave in the helical anisotropy vessel phantom also appears to propagate in a helical manner by rotating around the vessel wall with respect to the center of the vessel. Hence, positive or negative components will follow each other by turning around the phantom. This highly atypical pulse wave propagation can be put in perspective to the recent study published in Science where natural flexural pulse waves have been observed in human arteries [28].

The future clinical impacts of this finding are multiple. On the one hand, the propagation time angle of the Pulse wave could be used to evaluate the artery's anisotropy for early detection of atherosclerosis of atheroma plaque development, and rupture. Indeed, collagen fibers are essential structural components in various tissues and are primarily responsible for providing tissue strength [29]. Knowing that the strength of tissue is influenced by the orientation of the collagen [30] understanding the orientation of collagen fibrils in the atheroma plaque could be valuable in improving our knowledge of tissue vulnerability to rupture [31, 32]. On the other hand, considering the similarities between AK waves in the myocardium and pulse waves in arteries, these results suggest that such natural waves combined with the presented method could potentially be utilized to detect and image anisotropy in the myocardium.

5 Conclusion

Tubular phantoms were fabricated using PVA. By stretching and twisting the material, anisotropy was induced between two sets of two freeze-thaw cycles. Firstly, shear wave imaging was used to validate the process of fabricating an anisotropic vessel phantom. Subsequently, high frame rate 3D imaging was performed and used to detect the 3D propagation pattern of PW for each manufactured vessel phantom. The results suggest that vessel anisotropy affects pulse wave propagation. Finally, we propose to use the propagation angle which reflects the number of circumferential turns during vessel fabrication as a potential method to extract vessel anisotropy.

Data availability statement

The raw data supporting the conclusions of this article will be made available by the authors, without undue reservation.

Author contributions

JS: Data curation, Methodology, Software, Validation, Visualization, Writing–original draft, Writing–review and editing. SM: Data curation, Investigation, Methodology, Writing–review and editing. StF: Data curation, Methodology, Supervision, Writing–review and editing. MV: Conceptualization, Writing–review and editing. SoF: Writing–review and editing. LL: Writing–review and editing. OV: Writing–review and editing. Sebastien SS: Formal Analysis, Funding acquisition, Methodology, Project administration, Supervision, Writing–review and editing.

Funding

The author(s) declare that financial support was received for the research, authorship, and/or publication of this article. This work

was funded by ATIP AVENIR French grant received by Sebastien SS in 2022.

Conflict of interest

The authors declare that the research was conducted in the absence of any commercial or financial relationships that could be construed as a potential conflict of interest.

Publisher's note

References

1. Townsend N, Wilson L, Bhatnagar P, Wickramasinghe K, Rayner M, Nichols M. Cardiovascular disease in Europe: epidemiological update 2016. *Eur Heart J* (2016) 37(42):3232–45. doi:10.1093/eurheartj/ehw334

2. Emig R, Zgierski-Johnston CM, Timmermann V, Taberner AJ, Nash MP, Kohl P, et al. Passive myocardial mechanical properties: meaning, measurement, models. *Biophys Rev* (2021) 13(5):587–610. doi:10.1007/s12551-021-00838-1

3. Watson SR, Dormer JD, Fei B. Imaging technologies for cardiac fiber and heart failure: a review. *Heart Fail Rev* (2018) 23(2):273–89. doi:10.1007/s10741-018-9684-1

4. Villemain O, Correia M, Mousseaux E, Baranger J, Zarka S, Podetti I, et al. Myocardial stiffness evaluation using noninvasive shear wave imaging in healthy and hypertrophic cardiomyopathic adults. *JACC: Cardiovasc Imaging* (2018) 12:1135–45. doi:10.1016/j.jcmg.2018.02.002

5. Song P, Bi X, Mellema DC, Manduca A, Urban MW, Pellikka PA, et al. Pediatric cardiac shear wave elastography for quantitative assessment of myocardial stiffness: a pilot study in healthy controls. *Ultrasound Med and Biol* (2016) 42(8):1719–29. doi:10.1016/j.ultrasmedbio.2016.03.009

6. Wouters L, Duchenne J, Bézy S, Papangelopoulou K, Puvrez A, Klop B, et al. Septal scar detection in patients with left bundle branch block using echocardiographic shear wave elastography. *JACC: Cardiovasc Imaging* (2023) 16(5):713–5. doi:10.1016/j.jcmg.2022.11.008

7. Couade M, Pernot M, Prada C, Messas E, Emmerich J, Bruneval P, et al. Quantitative assessment of arterial wall biomechanical properties using shear wave imaging. *Ultrasound Med Biol* (2010) 36(10):1662–76. doi:10.1016/j.ultrasmedbio.2010.07.004

8. Ramnarine KV, Garrard JW, Kanber B, Nduwayo S, Hartshorne TC, Robinson TG. Shear wave elastography imaging of carotid plaques: feasible, reproducible and of clinical potential. *Cardiovasc Ultrasound* (2014) 12(1):49. doi:10.1186/1476-7120-12-49

9. Pislaru C, Alashry MM, Thaden JJ, Pellikka PA, Enriquez-Sarano M, Pislaru SV. Intrinsic wave propagation of myocardial stretch, A new tool to evaluate myocardial stiffness: a pilot study in patients with aortic stenosis and mitral regurgitation. *J Am Soc Echocardiogr* (2017) 30(11):1070–80. doi:10.1016/j.echo.2017.06.023

10. Vos HJ, van Dalen BM, Heinonen I, Bosch JG, Sorop O, Duncker DJ, et al. Cardiac shear wave velocity detection in the porcine heart. *Ultrasound Med and Biol* (2017) 43(4):753–64. doi:10.1016/j.ultrasmedbio.2016.11.015

11. Lee W-N, Pernot M, Couade M, Messas E, Bruneval P, Bel A, et al. Mapping myocardial fiber orientation using echocardiography-based shear wave imaging. *IEEE Trans Med Imaging* (2012) 31(3):554–62. doi:10.1109/TMI.2011.2172690

12. Salles S, Espeland T, Molares A, Aase SA, Hammer TA, Støylen A, et al. 3D myocardial mechanical wave measurements. *JACC: Cardiovasc Imaging* (2020) 14(8):1495–505. doi:10.1016/j.jcmg.2020.05.037

13. Kvåle KF, Salles S, Lervik LCN, Støylen A, Løvstakken L, Samset E, et al. Detection of tissue fibrosis using natural mechanical wave velocity estimation: feasibility study. *Ultrasound Med and Biol* (2020) 46(9):2481–92. doi:10.1016/j.ultrasmedbio.2020.04.022

14. Salles S, Lovstakken L, Torp H. *Ultrasound cardiac processing*. US 11497473 B2 (2022).

15. Salles S, Lovstakken L, Aase SA, Bjastad TG, Torp H. Clutter filter wave imaging. *IEEE Trans Ultrason Ferroelect, Freq Contr* (2019) 66(9):1444–52. doi:10.1109/tuffc.2019.2923710

16. Salles S, Aase SA, Bjastad T, Lovstakken L, Torp H. Clutter filter wave imaging (CFWI): a new way to visualize and detect mechanical waves propagation. In: 2017 IEEE International Ultrasonics Symposium (IUS). Washington, DC, USA: IEEE (2017). 1.

17. Vappou J, Luo J, Konofagou EE. Pulse wave imaging for noninvasive and quantitative measurement of arterial stiffness *in vivo*. *Am J Hypertens* (2010) 23(4):393–8. doi:10.1038/ajh.2009.272

18. Jianwen L, Li RX, Konofagou EE. Pulse wave imaging of the human carotid artery: an *in vivo* feasibility study. *IEEE Trans Ultrason Ferroelect, Freq Contr* (2012) 59(1):174–81. doi:10.1109/TUFFC.2012.2170

19. Rasouli R, Baranger J, Slorach C, Nguyen M, Segers P, Guerra V, et al. Local arterial stiffness assessment: comparison of pulse wave velocity assessed by ultrafast ultrasound imaging versus the bramwell-hill equation. *J Am Soc Echocardiography* (2022) 35(11):1185–8. doi:10.1016/j.echo.2022.07.011

20. Li RX, Apostolakis IZ, Kemper P, McGarry MDJ, Ip A, Connolly ES, et al. Pulse wave imaging in carotid artery stenosis human patients *in vivo*. *Ultrasound Med and Biol* (2019) 45(2):353–66. doi:10.1016/j.ultrasmedbio.2018.07.013

21. Apostolakis IZ, Nauleau P, Papadacci C, McGarry MD, Konofagou EE. Feasibility and validation of 4-D pulse wave imaging in phantoms and *in vivo*. *IEEE Trans Ultrason Ferroelect, Freq Contr* (2017) 64(9):1305–17. doi:10.1109/tuffc.2017.2735381

22. Fiorentini S, Sauvage J, Mostefaoui S, Lovstakken L, Salles S. Detection of natural pulse waves (PWs) for anisotropy characterization: an *in vitro* study. In: 2023 IEEE International Ultrasonics Symposium (IUS). Montreal, QC, Canada: IEEE (2023). 1–4.

23. Salles S, Chee AJY, Garcia D, Yu ACH, Vray D, Liebgott H. 2-D arterial wall motion imaging using ultrafast ultrasound and transverse oscillations. *IEEE Trans Ultrason Ferroelectr Freq Control* (2015) 62(6):1047–58. doi:10.1109/tuffc.2014.006910

24. Chatelin S, Bernal M, Deffieux T, Papadacci C, Flaud P, Nahas A, et al. Anisotropic polyvinyl alcohol hydrogel phantom for shear wave elastography in fibrous biological soft tissue: a multimodality characterization. *Phys Med Biol* (2014) 59(22):6923–40. doi:10.1088/0031-9155/59/22/6923

25. Millon LE, Mohammadi H, Wan WK. Anisotropic polyvinyl alcohol hydrogel for cardiovascular applications. *J Biomed Mater Res* (2006) 79B(2):305–11. doi:10.1002/jbm.b.30543

26. Rodriguez-Molares A, Rindal OMH, Bernard O, Nair A, Lediju Bell MA, Liebgott H, et al. The UltraSound ToolBox. In: 2017 IEEE International Ultrasonics Symposium (IUS). Washington, DC: IEEE (2017). 1–4.

27. He Q, Li GY, Lee FF, Zhang Q, Cao Y, Luo J. Novel method for vessel cross-sectional shear wave imaging. *Ultrasound Med and Biol* (2017) 43(7):1520–32. doi:10.1016/j.ultrasmedbio.2017.03.001

28. Laloy-Borgna G, Puyo L, Nishino H, Atlan M, Catheline S. Observation of natural flexural pulse waves in retinal and carotid arteries for wall elasticity estimation. *Sci Adv* (2023) 9(25):eadf1783. doi:10.1126/sciadv.adf1783

29. Fratzl P, editor. *Collagen: structure and mechanics, an introduction*. Boston, MA: Springer US (2008). 1–13.

30. Whelan A, Duffy J, Gaul RT, O'Reilly D, Nolan DR, Gunning P, et al. Collagen fibre orientation and dispersion govern ultimate tensile strength, stiffness and the fatigue performance of bovine pericardium. *J Mech Behav Biomed Mater* (2019) 90:54–60. doi:10.1016/j.jmbbm.2018.09.038

31. Silva H, Tassone C, Ross EG, Lee JT, Zhou W, Nelson D. Collagen fibril orientation in tissue specimens from atherosclerotic plaque explored using small angle X-ray scattering. *J Biomechanical Eng* (2022) 144(2):024505. doi:10.1115/1.4052432

32. Douglas GR, Brown AJ, Gillard JH, Bennett MR, Sutcliffe MPF, Teng Z. Impact of fiber structure on the material stability and rupture mechanisms of coronary atherosclerotic plaques. *Ann Biomed Eng* (2017) 45(6):1462–74. doi:10.1007/s10439-017-1827-3